# Stability of a Liquid Jet Impinging on Confined Saturated Sand

Jérémy Vessaire,[1] Germán Varas,[2] Sylvain Joubaud,[1,3] Romain Volk,[1] Mickaël Bourgoin,[1] and Valérie Vidal[1,*]
[1]Univ Lyon, ENS de Lyon, Univ Lyon 1, CNRS, Laboratoire de Physique, F-69342 Lyon, France
[2]Instituto de Física, Pontificia Universidad Católica de Valparaíso (PUCV), 2340000 Valparaíso, Chile
[3]Institut Universitaire de France, 1 rue Descartes, 75005 Paris, France

(Received 3 October 2019; revised manuscript received 7 January 2020; accepted 11 May 2020; published 2 June 2020)

This Letter focuses on the dynamics of a liquid jet impacting the surface of a confined, immersed granular bed. Although previous works have considered the erosion process and surface morphology, less attention has been given to the jet hydrodynamics. Based on laboratory experiments, we show that when the liquid jet forms a crater, two situations arise. For weak or no erosion and for open craters, the jet is stationary. For vertical or overhanging crater walls, the jet displays a wide range of behaviors, from quasiperiodic oscillations to symmetry breaking and exploration of different states in time. An analysis of the different system states leads to the emergence of a bifurcation diagram depending on a dimensionless parameter, $J$, comparing the jet impact force to the force necessary to eject a grain. The frequency of the jet oscillations depends on the inertial velocity, the jet dispersion and the ratio between the injector cross section and the confinement length.

DOI: 10.1103/PhysRevLett.124.224502

Crater formation by impacting a granular material is ubiquitous in nature, from raindrops falling on sandy deserts to meteorites impacting moons and planets. Due to the complexity of the underlying physical mechanisms, it has raised the curiosity of scientists since more than a century (see [1,2] and references therein). In the last decades, however, the human race to space and deep oceans has brought forward new challenges related to the formation of craters by impinging jets. On the one hand, since the Apollo and Viking programs, erosion and cratering mechanisms have focused great interest as they have direct consequences on hazards for retrograde rockets landing on planetary regoliths—reduced visibility, vehicle damage, or uneven landing surface [3–7]. On the other hand, recent technical developments for either space exploration or deep-sea mining allow mineral extraction by impacting jets [8–11], such as the Touch-and-Go Sample Acquisition Mechanism (TAGSAM) for asteroid sampling [12]. Understanding and quantifying the mechanisms at stake is not only a challenge for hazard mitigation but also, for deep-sea mining, a crucial need to assess potential environmental effects of large-scale sediments resuspension [8,9,13,14]. Since the pioneering work of Aderibigbe *et al.* [15], many studies of two-phase systems with gas or liquid jets eroding a dry or immersed granular bed have proposed an accurate description of the erosion threshold, bedload transport, or crater morphology [6,16–22]. However, less attention has been given to the possible appearance of flow instabilities, which may lead to drastic consequences for lunar, planetary, or asteroid landing hazards. Metzger *et al.* pointed out crater depth oscillations, which seem to "correlate to periodic avalanching of the outer crater" [4]. Later on, Clark and Behringer reported a horizontal symmetry breaking when "the sidewalls of the inner crater range from nearly vertical to overhanging and a circular-like flow pattern emerges," leading to strongly asymmetric craters [6]. However, to our knowledge, none of these studies focused on the dynamics of the jet itself. Yet it is well known, since the first observation of the edge-tone phenomenon by Sondhaus in 1854 [23], that jets impacting on a solid obstacle or confined in a cavity can develop self-sustained oscillations [24–32]. Do these oscillations arise when the jet impacts a porous medium? What is the coupling with crater morphology? The present work focuses on the stability of a liquid jet when impacting a confined saturated granular bed. We quantify both the jet hydrodynamics and the soil surface morphology, and demonstrate the appearance of a new instability, based on the fluid-particles coupling.

The experimental device consists of a Hele-Shaw cell (40 cm width, 15 cm height, gap $e = 2.2$ mm) partially filled with glass beads (Sovitec glass spheres) of diameter $d = 750$ $\mu$m, immersed in water. The particles have a density $\rho_p = 2300\ \mathrm{kg\,m^{-3}}$ and a density difference $\Delta\rho = \rho_p - \rho_f$ with the surrounding fluid, with $\rho_f = 1000\ \mathrm{kg\,m^{-3}}$. In all experiments, the granular layer height is fixed to 5 cm so that the maximum of the scour is always far from cell bottom. Between each experiments, the grains are stirred gently and then leveled with a ruler to obtain a horizontal free surface. This protocol ensures reproducible results. Four different impingement heights $h = [1, 3, 5, 8]$ cm are used. A homemade push syringe generates a water jet at constant flow-rate $Q$ through a cylindrical injector of inner diameter 1.4 mm (cross

 

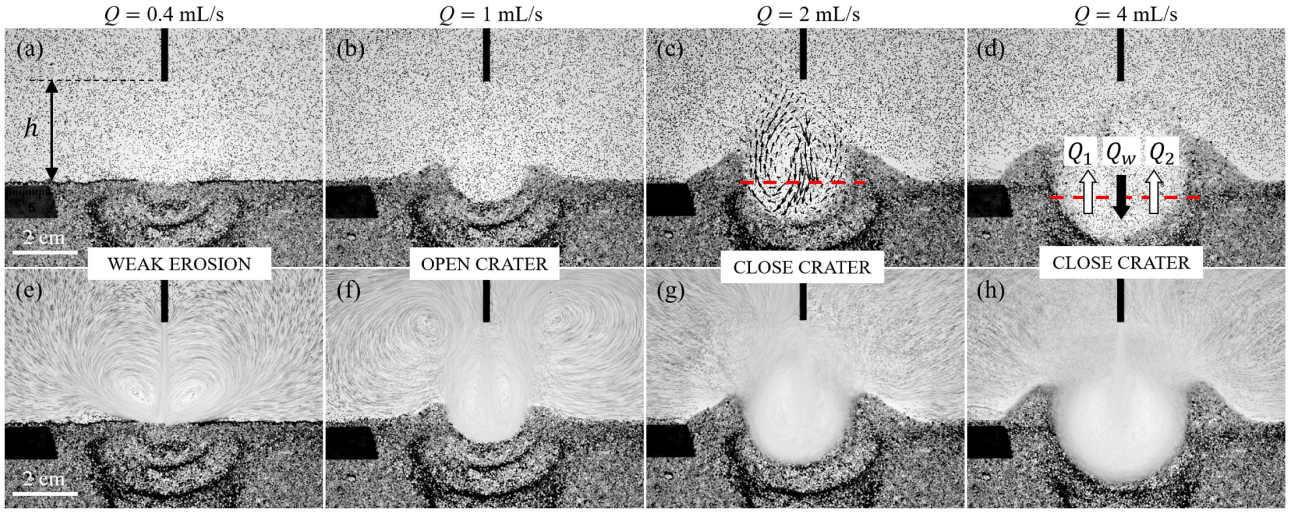


FIG. 1. Crater morphology for different liquid flow rates $Q$ [$h = 3$ cm]. The upper panels (a)–(d) show a snapshot and the lower panels (e)–(h) display the average over the last 1000 images. Panel (c) shows an example of PIV computation. The red dashed lines in (c),(d) display the section upon which the incident (downward) flux $Q_w$ and the upward side fluxes $Q_1$ and $Q_2$ are computed.

sectional area $S$) located at a height $h$ above the granular bed. The water level remains constant and well above the injector throughout the entire experiment using an exhaust hole located at the top of the cell. To perform particle image velocimetry (PIV) analysis, the liquid is seeded with isodense tracers (Cospheric, diameter 212 $\mu$m). Comparison with experiments without tracers show that they do not affect the erosion process and crater morphology. Images are recorded with a fast camera (Phantom Miro M110) at 1600 fps (size $768 \times 1024$ pix$^2$), and the PIV field is computed by means of the open source code PIVLab [33,34]. The contrast between the tracers and the background and glass beads is increased by means of a contrast limited adaptive histogram equalization (CLAHE) algorithm for each image. To get the largest velocity range from the nozzle to the crater bottom, a multipass PIV method with an interrogation window from $128 \times 128$ to $16 \times 16$ pixels is applied. Finally, to check the reproducibility and increase the statistics, each experiment with fixed parameters $(h, Q)$ is repeated five times.

At low flow-rate $Q$ and large $h$, the liquid jet is not strong enough to form a crater [Fig. 1(a)]. As the jet speed increases or the impingement height decreases, a crater is formed [Figs. 1(b)–1(d)]. After a rapid transient, the crater morphology reaches a state in which it only evolves slowly in time (see the Supplemental Material A.1 and Fig. S1 [35]). Figure 2 displays the crater morphology in this latter regime, in the parameters space $(h, Q)$. We recover the classical morphologies described in the literature [15]: weak (square) or no erosion (cross), strongly deflected jet regimes, which generate a peculiar crater morphology resembling an indentation [(plus), see the Supplemental Material A.2 [35]], or well-developed craters (central and bottom pictures, inset Fig. 2). The open craters (inverted triangle) are distinguished from the close craters (circle) by analyzing both the movies and the average intensity over the last 1000 images. Craters are defined as close when the angle between the horizontal and at least one of their inner walls is equal or larger than 90° (vertical or overhanging wall, see the Supplemental Material A.3 [35]). This criterion matches with the observation for open craters of buckling streamlines on each side of the impacting jet, due to the return flow which is not trapped inside the crater [Figs. 1(e) and 1(f)].

Coupling PIV analysis of the fluid flow and crater morphology evidences a region where the impinging jet

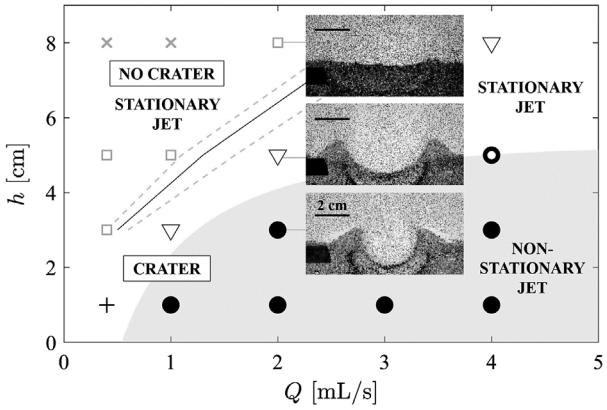


FIG. 2. Crater morphology and jet stability in the phase space $(Q, h)$. (Cross) no erosion; (Square) weak erosion; (Plus) jet indentation; (Inverted triangle) open crater; (Circle) close crater with stationary (black and white) or nonstationary (black) jet. Solid black line: $J = 0.6$ [Eq. (1)] for the jet angle determined experimentally, with error estimation (dashed gray lines). The gray zone (guide for the eye) shows the existence of jet oscillations.

does not have the classical self-similar profile and displays a non-stationary behavior (Fig. 2, gray region). We denote $Q_w$ the incident flux and $Q_i$ $(i = 1, 2)$ the reflected fluxes on each side of the incident jet, computed as the spatial average of the downward and upward liquid flows through the horizontal line at the center of the crater [Fig. 1(d)].

Figures 3(a)–3(d) display the time evolution of $Q_1$ and $Q_2$ for different jet dynamics. Granular layers with no erosion or open craters are characterized by a stationary jet, with symmetric fluxes [Fig. 3(a)]. Jets in close craters, on the contrary, exhibit a wide range of dynamics, from fully asymmetric [Fig. 3(b)] to symmetric with self-sustained oscillations [Fig. 3(d)], including the exploration of different states in time [Fig. 3(c)]. A system state is defined as a constant mean value of $Q_{1,2}$, superimposed with fluctuations. Note that except for fully asymmetric states, jets in close craters always exhibit fluctuations or quasiperiodic oscillations of $Q_1$ and $Q_2$ in phase opposition, corresponding to lateral displacements of the incident jet. The typical time of these oscillations or states exploration is of the order of 0.1 to 1 s, during which the global crater morphology does not exhibit any significant change (see the Supplemental Material [35], Fig. S1).

To characterize the system dynamics, we introduce a dimensionless parameter adapted from the erosion parameter $E$ previously defined for submerged impinging circular jets as the ratio between the force exerted by the impacting jet on a bed particle located under the jet at the original bed surface to its resistive force [15]. It is adapted here to the confined geometry and scales as the velocity ratio of the jet impacting the initial bed surface and the particle velocity:

$$J = \frac{Q}{(2eh\tan\alpha)u}, \tag{1}$$

where $u = \sqrt{(\Delta\rho/\rho_f)gd}$ is the inertial particle velocity corrected from buoyancy effects with $g$ the gravitational acceleration and $\alpha$ the half-angle of the liquid jet. Note that $J$ corresponds to the square root of a Shields number based on the average velocity of the jet impacting the initial bed surface. The jet half-angle $\alpha$ is measured experimentally for each $(h, Q)$ in the absence of a granular layer, $h$ corresponding here to the distance between the injection nozzle and the horizontal wall at the cell bottom (see the Supplemental Material [35], A.4). As already proposed in the literature [15], the critical value $J \simeq 0.6$ captures well the transition between weak or no erosion, and the formation of a crater (Fig. 2, solid black line). In the following, we will consider the average angle evolution as a function of the flow rate, $\alpha = \alpha_0 + (\alpha^* - \alpha_0)Q/Q_c$ for $Q \leq Q_c$ and $\alpha = \alpha^*$ for $Q \geq Q_c$, with $\alpha_0 = 3°$, $\alpha^* = 6.5°$ and $Q_c = 2$ mL/s ([35] Fig. S4, dashed line).

The exploration of different system states is quantified by introducing an asymmetry parameter, $\xi$, defined for each

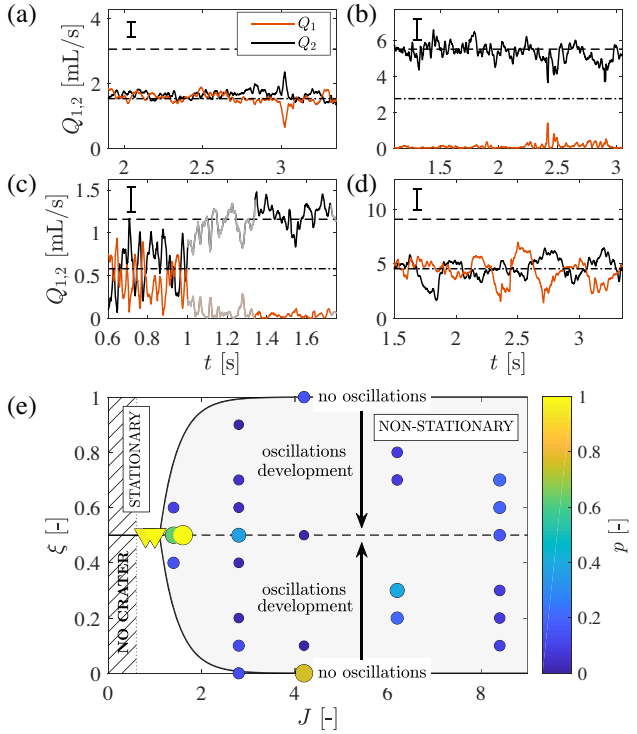


FIG. 3. (a)–(d) Different flow regimes [$Q_1$, orange; $Q_2$, black; $\langle Q_w \rangle$, dashed where $\langle . \rangle$ denotes the time average (error bar = standard deviation of $\langle Q_w \rangle$ fluctuations); $\langle Q_w/2 \rangle$, dash-dotted] ($h$[cm], $Q$[mL/s], $J$). (a) Symmetric (3,1,0.95); (b) asymmetric (1,2,4.18); (c) different states (1,1,2.86), the gray parts of the signals indicate the transition regions; (d) quasiperiodic oscillations (3,4,2.78). (e) System asymmetry $\xi$ as a function of $J$. Hatched region: no crater formation, inverted triangles = open craters, circles = close craters. Gray zone: nonstationary jet that explores different states. The colorscale gives the probability $p$ for the system to be in a state $\{\xi\}$ for a given $J$.

system state as $\langle Q_1 \rangle / \langle Q_1 + Q_2 \rangle$ where $\langle . \rangle$ indicates the time average of the signal. We exclude here the transition regions. For $\xi = 0.5$, $\langle Q_1 \rangle = \langle Q_2 \rangle$, while for $\xi = 0$ or 1, all the upward flow is locked on one side of the crater (fully asymmetric jet). All experiments corresponding to a same value of the dimensionless parameter $J$ are concatenated, so we can estimate not only the different system states, but also the probability $p$ of the system to explore such state in time. In addition, $\xi$ is divided in bins of width 0.1, meaning that two states in the same bin are attributed the same $\xi$ value. Figure 3(e) summarizes the system states and liquid jet dynamics when increasing $J$. The markers size and color indicate the probability of the system to be in the state of value $\xi$, while the symbols indicate the crater geometry (open or close). Open craters [Fig. 3(e), inverted triangles] always display a stationary behavior, symmetric fluxes and $\xi = 0.5$. Close craters [Fig. 3(e), circles], on the contrary, display nonstationary fluxes and explore different states in time. The transition from a stationary to a nonstationary jet occurs through a bifurcation diagram, with a transition at

$J^* \simeq 1$. In the nonstationary regime, the system has an almost equal probability to explore the different states. The lack of data points for some $J$ (for instance $J \simeq 4$) is the consequence of the lack of statistics. Although binning $\xi$ makes possible in most cases to increase the statistics, it would require more or longer experiments to explore the whole range of $\xi$ expected from this figure.

When the jet is fully asymmetric ($\xi = 0$ or 1), it does not display oscillations. Oscillations develop gradually when $|\xi - 1/2|$ decreases to zero [Fig. 3(e), black arrows], until steady, quasiperiodic oscillations appear for $\xi = 0.5$ [Fig. 3(d)]. The oscillation frequency is quantified by performing the cross correlation of the flow-rate fluctuations $(Q_1 - \langle Q_1 \rangle)$ with $(Q_2 - \langle Q_2 \rangle)$. Figure 4(a), inset, displays the oscillations frequency as a function of $J$, in the region where they develop ($J > J^*$, gray region). The gray crosses indicate the frequency for each experiment, and the black star their average for the same $J$. To scale the frequency, we introduce the global Strouhal number $\mathrm{St} = fL/V$ based on the jet velocity at the injector outlet, $V = Q/S$, and on the impingement length $L = h$ [24]. St exhibits a power-law behavior as a function of $J$, $\mathrm{St} = \beta J^{\gamma}$ with $\gamma \simeq -1$ and $\beta \simeq 0.09$ [Fig. 4(a)]. Rewriting this law using Eq. (1) provides the frequency evolution as a function of the system's parameters:

$$f = 2\beta \left( \frac{u}{S/e} \right) \tan \alpha. \tag{2}$$

The oscillation frequency is therefore driven by the particle inertial velocity $u$, including buoyancy correction, the jet dispersion $\alpha$ and the ratio between the injector cross section $S$ and the confinement length $e$. It only depends indirectly on the jet speed at the outlet through the jet half-angle $\alpha$. The dashed line in Fig. 4, inset, corresponds to the frequency computed from Eq. (2) with $\alpha = \alpha^*$ (see the Supplemental Material [35], A.4), which is the case for most experiments showing oscillations ($Q \geq Q_c$). It captures successfully the order of magnitude ($\simeq$2.7 Hz) of the observed frequency, using the empirical parameter $\beta \simeq 0.09$.

The appearance of self-sustained oscillations for confined jets impinging an obstacle is commonly explained as a feedback mechanism resulting in the formation of a large, coherent structure [24,25,28,30,31]. Two possible mechanisms, acoustic or hydrodynamic, can be at the origin of the feedback loop: (1) the impinging jet generates acoustic waves that propagate upstream and interact with the nozzle; (2) downstream-convected structures are advected by a recirculation flow and force in-phase oscillations at the nozzle exit. These mechanisms, however, are not at stake here for the following reasons. (1) The acoustic feedback loop is characterized, at a low Mach number, by a constant Strouhal number [30], which discards this origin for the observed oscillations. (2) Feedback effect due to the growth and recirculation of flow disturbances generates oscillations whose frequency increases with the jet speed [27], which is not observed in our experiments.

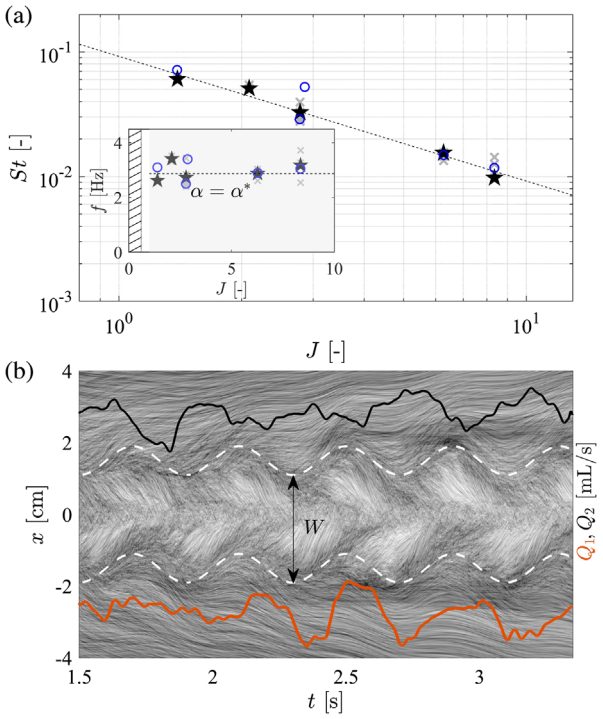


FIG. 4. (a) Strouhal number St as a function of $J$ [(crosses) from fluxes cross-correlation, (stars) data from fluxes averaged for a given $J$, (circles) from spatiotemporal]. The error bar is smaller than each symbol size. Dashed line: fit of the average values, $\mathrm{St} = \beta J^{-1}$ with $\beta \simeq 0.09$. Inset: jet oscillation frequency $f$. Hatched region: no or weak erosion; gray area: oscillations. Dashed line: frequency given by Eq. (2) for $\alpha = \alpha^*$. (b) Spatiotemporal evolution of the images intensity along a horizontal region encompassing the crater aperture. The crater aperture width $W$ is visible as the clear, oscillating region [$h = 3$ cm, $Q = 4$ mL/s]. Orange and black lines: data $Q_1$ and $Q_2$ from Fig. 3(d), vertically shifted for clarity. White dashed lines: harmonic oscillations at 2.5 Hz (guides for the eye).

Figure 4(b) presents the spatiotemporal evolution of the images intensity along a horizontal section of about 1 cm height encompassing the crater aperture. Each column is the average over the section height, and $x = 0$ is at the vertical of the nozzle. The crater aperture width, $W$, exhibits clear oscillations, here with a frequency of about 2.5 Hz (white dashed lines), similar to the jet flow oscillations (2.44 Hz for this experiment). We report in Fig. 4(a) the frequency inferred from the spatiotemporal diagram (blue circles) for different $J$. It matches quite fairly the frequency obtained from the flux signals analysis. These oscillations thus correspond to the quasiperiodic motion of grains forming the dunes at the crater aperture, visible in Fig. 1(d). The self-sustained oscillations are therefore generated by a coupling between the fluid and grains, which explains why the frequency is almost independent on

the jet speed ($\alpha = \alpha^*$ in most experiments with oscillations) but strongly depends on the inertial particle velocity $u$.

Impinging jets over deformable granular beds in confined environment thus lead to the appearance of flow oscillations for close crater geometries. Although further dependence with the confinement should be assessed, this Letter shows that the strong coupling between fluid and particles is responsible for this instabilities generation, which could be responsible for safety failure in many practical situations.

This work was supported by Programa de Cooperación Científica ECOS/CONICYT C14E07, the Laboratoire International Associé "Matière: Structure et Dynamique" (LIA-MSD, France-Chile), the French research program ANR-16-CE30-0028 and IDEXLYON of the University of Lyon in the framework of the French program "Programme Investissements d'Avenir" (ANR-16-IDEX-0005). The authors wish to thank the two anonymous referees for fruitful discussions which greatly improved this manuscript.

*Corresponding author.
valerie.vidal@ens-lyon.fr

[1] A. M. Walsh, K. E. Holloway, P. Habdas, and J. R. de Bruyn, Phys. Rev. Lett. **91**, 104301 (2003).
[2] D. van der Meer, Annu. Rev. Fluid Mech. **49**, 463 (2017).
[3] L. Roberts, in *A Compilation of Recent Research Related to the Apollo Mission* (National Aeronautics and Space Administration, Hampton, VA, 1963), pp. 155–170.
[4] P. T. Metzger, C. D. Immer, C. M. Donahue, B. T. Vu, R. C. Latta, and M. Deyo-Svendsen, J. Aerospace Eng. **22**, 24 (2009).
[5] K. J. Berger, A. Anand, P. T. Metzger, and C. M. Hrenya, Phys. Rev. E **87**, 022205 (2013).
[6] A. H. Clark and R. P. Behringer, Granul. Matter **16**, 433 (2014).
[7] J. E. Lane and P. T. Metzger, Acta Geophys. **63**, 568 (2015).
[8] H. U. Oebius, H. J. Becker, S. Rolinski, and J. A. Jankowski, Deep-Sea Research, Part II **48**, 3453 (2001).
[9] G. Schriever and H. Thiel, in *Proceedings of the Tenth (2013) ISOPE Ocean Mining and Gas Hydrates Symposium* (The International Society of Offshore and Polar Engineers (ISOPE), Szczecin, Poland, 2013), pp. 5–17, https://www.researchgate.net/publication/287237214_Tailings_and_their_disposal_in_deep-sea_mining/link/58aee1e8a6fdcc6f03f32b75/download.
[10] S. Tachibana, M. Abe, M. Arakawa, M. Fujimoto, Y. Iijima, M. Ishiguro, K. Kitazato, N. Kobayashi, N. Namiki, T. Okada, R. Okazaki, H. Sawada, S. Sugita, Y. Takano, S. Tanaka, S. Watanabe, M. Yoshikawa, and H. Kuninaka (The Hayabusa2 Project Team), Geochem. J. **48**, 571 (2014).
[11] T. Saiki, H. Imamura, M. Arakawa, K. Wada, Y. Takagi, M. Hayakawa, K. Shirai, H. Yano, and C. Okamoto, Space Sci. Rev. **208**, 165 (2017).
[12] E. B. Bierhaus, B. C. Clark, J. W. Harris, K. S. Payne, R. D. Dubisher, D. W. Wurts, R. A. Hund, R. M. Kuhns, T. M. Linn, J. L. Wood, A. J. May, J. P. Dworkin, E. Beshore, and D. S. Lauretta (The OSIRIS-REx Team), Space Sci. Rev. **214**, 107 (2018).
[13] H. J. Becker, B. Grupe, H. U. Oebius, and F. Liu, Deep-Sea Research, Part II **48**, 3609 (2001).
[14] T. Peacock and M. H. Alford, Sci. Am. **318**, 72 (2018).
[15] O. Aderibigbe and N. Rajaratnam, J. Hydraul. Res. **34**, 19 (1996).
[16] P. T. Metzger, R. C. Latta, J. M. Schuler, and C. D. Immer, AIP Conf. Proc. **1145**, 767 (2009).
[17] P. Aussillous, J. Chauchat, M. Pailha, M. Médale, and E. Guazzelli, J. Fluid Mech. **736**, 594 (2013).
[18] S. Badr, G. Gauthier, and P. Gondret, Phys. Fluids **26**, 023302 (2014).
[19] B. R. Sutherland and S. Dalziel, Phys. Fluids **26**, 035103 (2014).
[20] C. Q. Lamarche and J. Sinclair Curtis, Chem. Eng. Sci. **138**, 432 (2015).
[21] S. Badr, G. Gauthier, and P. Gondret, Phys. Fluids **28**, 033305 (2016).
[22] M. Houssais, C. P. Ortiz, D. J. Durian, and D. J. Jerolmack, Phys. Rev. E **94**, 062609 (2016).
[23] C. Sondhaus, Ann. Phys. (Berlin) **167**, 214 (1854).
[24] D. Rockwell and E. Naudascher, Annu. Rev. Fluid Mech. **11**, 67 (1979).
[25] C. M. Ho and N. S. Nosseir, J. Fluid Mech. **105**, 119 (1981).
[26] D. Rockwell, AIAA J. **21**, 645 (1983).
[27] E. Villermaux and E. Hopfinger, Physica (Amsterdam) **72D**, 230 (1994).
[28] A. Maurel, P. Ern, B. J. A. Zielinska, and J. E. Wesfreid, Phys. Rev. E **54**, 3643 (1996).
[29] B. M. Gebert, M. R. Davidson, and M. J. Rudman, Appl. Math. Model. **22**, 843 (1998).
[30] D. Varieras, P. Brancher, and A. Giovannini, Flow Turbul. Combust. **78**, 1 (2007).
[31] B. W. Righolt, S. Kenjereš, R. Kalter, M. J. Tummers, and C. R. Kleijn, Phys. Fluids **27**, 095107 (2015).
[32] Y. Li and X. Ming, Eur. J. Mech. B **57**, 40 (2016).
[33] W. Thielicke and E. J. Stamhuis, J. Open Res. Software **2**, e30 (2014).
[34] W. Thielicke and E. J. Stamhuis, PIVlab—Time-Resolved Digital Particle Image Velocimetry Tool for MATLAB (version: 2.02) (2014), http://dx.doi.org/10.6084/m9.figshare.1092508.
[35] See the Supplemental Material at http://link.aps.org/supplemental/10.1103/PhysRevLett.124.224502 for the temporal evolution of the crated morphology, the peculiar regime of jet indentation, movies corresponding to the four examples displayed in Fig. 1 and the determination of the jet angle.